INTERFACE

rsif.royalsocietypublishing.org

Research

Cite this article: Bode-Oke AT, Zeyghami S, Dong H. 2018 Flying in reverse: kinematics and aerodynamics of a dragonfly in backward free flight. *J. R. Soc. Interface* **15**: 20180102. http://dx.doi.org/10.1098/rsif.2018.0102

Received: 9 February 2018
Accepted: 5 June 2018

Subject Category:
Life Sciences–Engineering interface

Subject Areas:
biomechanics, biomimetics, biophysics

Keywords:
backward flight, downstroke–upstroke reversal, active upstroke, leading edge vortex, dragonfly, force asymmetry

Author for correspondence:
Haibo Dong
e-mail: haibo.dong@virginia.edu

†Present address: Mechanical Engineering and Mechanics, Lehigh University, Bethlehem, PA 18015, USA.

Electronic supplementary material is available online at https://dx.doi.org/10.6084/m9.figshare.c.4131254.

THE ROYAL SOCIETY PUBLISHING

Flying in reverse: kinematics and aerodynamics of a dragonfly in backward free flight

Ayodeji T. Bode-Oke, Samane Zeyghami† and Haibo Dong

Mechanical and Aerospace Engineering, University of Virginia, Charlottesville, VA 22903, USA

ATB-O, 0000-0002-2746-1822; HD, 0000-0001-7823-7014

In this study, we investigated the backward free flight of a dragonfly, accelerating in a flight path inclined to the horizontal. The wing and body kinematics were reconstructed from the output of three high-speed cameras using a template-based subdivision surface reconstruction method, and numerical simulations using an immersed boundary flow solver were conducted to compute the forces and visualize the flow features. During backward flight, the dragonfly maintained an upright body posture of approximately 90° relative to the horizon. The upright body posture was used to reorient the stroke plane and the flight force in the global frame; a mechanism known as 'force vectoring' which was previously observed in manoeuvres of other flying animals. In addition to force vectoring, we found that while flying backward, the dragonfly flaps its wings with larger angles of attack in the upstroke (US) when compared with forward flight. Also, the backward velocity of the body in the upright position enhances the wings' net velocity in the US. The combined effect of the angle of attack and wing net velocity yields large aerodynamic force generation in the US, with the average magnitude of the force reaching values as high as two to three times the body weight. Corresponding to these large forces was the presence of a strong leading edge vortex (LEV) at the onset of US which remained attached up until wing reversal. Finally, wing–wing interaction was found to enhance the aerodynamic performance of the hindwings (HW) during backward flight. Vorticity from the forewings' trailing edge fed directly into the HW LEV to increase its circulation and enhance force production.

1. Introduction

Insects elicit flight manoeuvres by drastically or subtly changing their wing and body kinematics. These changes influence both (i) the production and (ii) orientation and reorientation of aerodynamic forces, consequently determining the type of free flight manoeuvre that is performed. Examples of such manoeuvres include well-studied modes like hovering, forward and turning flight [1–6], which have improved our understanding of flight mechanics and for engineers especially, fostered the design of micro-aerial vehicles (MAVs) [7–9]. However, some flight modes found in nature which may lead to further insights are yet to be explored. A classic example is backward flight. Although just qualitatively characterized in the literature, it has been documented that insects use backward flight for predator evasion, prey capture, flight initiation, station keeping and load lifting [10–15]. Now, engineers are interested in incorporating retro-flight capabilities into state-of-the-art MAVs for additional manoeuvrability [9,16]. To better understand the aerodynamics of backward flight in connection with wing and body kinematics, we studied free flying dragonflies in this flight mode.

First, to fly, insects need to produce forces by controlling both the velocity of and circulation generated by their wings [5,17,18]. Because force production is proportional to wing velocity squared, insects adjust wing speed by altering the stroke amplitude and/or frequency [5,11,17]. Honeybees [18], drone flies [19], damselflies [20] and fruit flies [21] all increase stroke amplitude to generate

Table 1. Morphological parameters for the dragonfly in this study. The mass and length measurement uncertainties are ± 1 mg and ± 1 mm, respectively.

species	flight time (ms)	body weight (mg)	body length (mm)	forewing length (mm)	forewing mean chord (mm)	hindwing length (mm)	hindwing mean chord (mm)	flapping frequency (Hz)
Erythemis simplicicollis	130	130	40	34	8	31	10	27

larger flight forces. Insects also modulate the circulation produced by their wings by controlling the angle of attack (AoA) with wing flexibility and rotation speed playing lesser roles [17]. When a wing flaps at a high AoA, the flow separates at the leading edge and reattaches before the trailing edge, forming a vortex which stays stably attached to wing due to the balance of centripetal and Coriolis accelerations [22]. The presence of the leading edge vortex (LEV) in insect flight has been associated with enhanced forces on the wing [10,23]. Although there are different views on how the existence and attachment of the LEV contribute to force production in insect flight (absence of stall [24], increasing wing circulation/suction [25], etc.), it is known that a wing with an LEV imparts greater momentum to the fluid, leading to the production of larger forces than under steady-state conditions [26–29]. Bomphrey *et al*. [30] measured the LEV contribution to weight support during the forward flight of dragonflies and concluded that dragonflies could sustain their weight from the contribution of the LEV on the forewings (FW) alone. Since the flight forces are a strong function of wing kinematics, generated flight forces vary drastically during flight because the kinematics of the upstroke (US) and downstroke (DS) can be utterly different [3,20,31]. In hovering and forward flight, most insects, especially those which flap in an inclined stroke plane, i.e. dragonflies, damselflies, etc. produce larger forces during the DS due to the higher relative wing velocity and the AoA in comparison to the US [31,32]. Conversely, the wing translates at a shallow AoA and smaller speed, tracing a shorter path in the US, thus, generating smaller forces [8,20,32]. The US is often 'aerodynamically inactive' as a result [20]. Currently, the variation of forces on a half-stroke basis and the roles of the US and DS in force generation during backward flight are less understood.

Second, the orientation and reorientation of aerodynamic forces is as essential for successful flight as force production and is vital to positioning the insect in its intended flight direction. Many flying organisms such as cicadas [33], fruit flies [4], dipterans [34], bats [35] and pigeons [36] use force vectoring like a helicopter for force reorientation. Force vectoring involves redirecting flight forces globally by rotating the body while the force vector remains relatively fixed to the body. A helicopter rotates the force vector by inducing a nose-down motion on the fuselage and tilting the tip-path plane (of the blades) forward to induce forward flight. Conversely, to transition to backward flight, a helicopter rotates the force vector by inducing a nose-up motion on the fuselage and tilts the tip-path plane backward. Most of the tilt is accomplished through fuselage rotation because the tilt of the tip-path is limited by the range of motion of the swash plates. Similarly, a tilt of the stroke plane has been reported to precede changes in the flight direction of insects [32]. Dragonflies, which have been reported to have a limited range of variation of the stroke plane with respect to their bodies [37], maintain a pitch-down orientation during forward flight. Like helicopters, flying backward in insects may require a similar strategy where the insect will maintain a pitch-up orientation. Rüppell [11] recorded a dragonfly flying backward with a body angle of 100° from the horizon. Likewise, Mukundarajan *et al*. [38] reported that a stroke plane tilted backward, and a steep body angle between 50° and 70° from the horizontal induced backward flight in waterlily beetles (*Galerucella nymphaeae*). Our observations corroborate these reports as we consistently witnessed an upright body posture during the backward flight of dragonflies in our experiment.

In the present work, our goal is to investigate the kinematics and aerodynamics of a dragonfly in backward flight. More precisely, we aim to identify the role that force vectoring plays in the execution of a backward flight manoeuvre. Furthermore, we will identify other aerodynamic mechanisms related to backward flight, if any, and quantify their contributions with regard to this unique flight mode. An accurate three-dimensional (3D) surface reconstruction technique coupled with a high-fidelity computational fluid dynamics (CFD) flow solver [39] is used to quantify the coordination of the wing and body motion and to identify how flight forces are generated during flight. Also, detailed flow features are elucidated and their relations to force generation mechanisms are evaluated and presented.

2. Material and methods

2.1. Dragonfly, high-speed videography and three-dimensional surface reconstruction

We captured dragonflies (*Erythemis simplicicollis*) from the wild and transported them to the laboratory for motion capture. We dotted the dragonflies' wings for tracking purposes and placed the insects in a filming area. The insects initiated flight voluntarily, and their motion was recorded by three orthogonally arranged high-speed cameras. While many of the flight sequences were of forward motions, we captured 10 backward flight videos. These backward sequences included turning and straight backward flight, very short backward flight after take-off and backward flight of individuals with impaired wings. Our aim in this work is to present the best and clearest straight backward flight sequence we captured for analysis in the text. We selected one flight sequence and reconstructed the video in Autodesk Maya (Autodesk Inc.). The morphological parameters of the selected dragonfly are shown in table 1, and the flight video can be found in the electronic supplementary material. The reconstruction process captured both the kinematics and deformations. A more detailed study of the 3D reconstruction method is identified elsewhere [40].

2.2. Wing kinematics and deformation

The wing kinematics are measured with respect to a coordinate system fixed at the wing root. Three Euler angles describe the angular orientation of the wing assuming it is rigid; flap, deviation and pitch. The effective AoA (α_{eff}) here is the angle between the chord and the vector sum of the body and wing velocity measured at the leading edge. Previous insect flight studies have measured

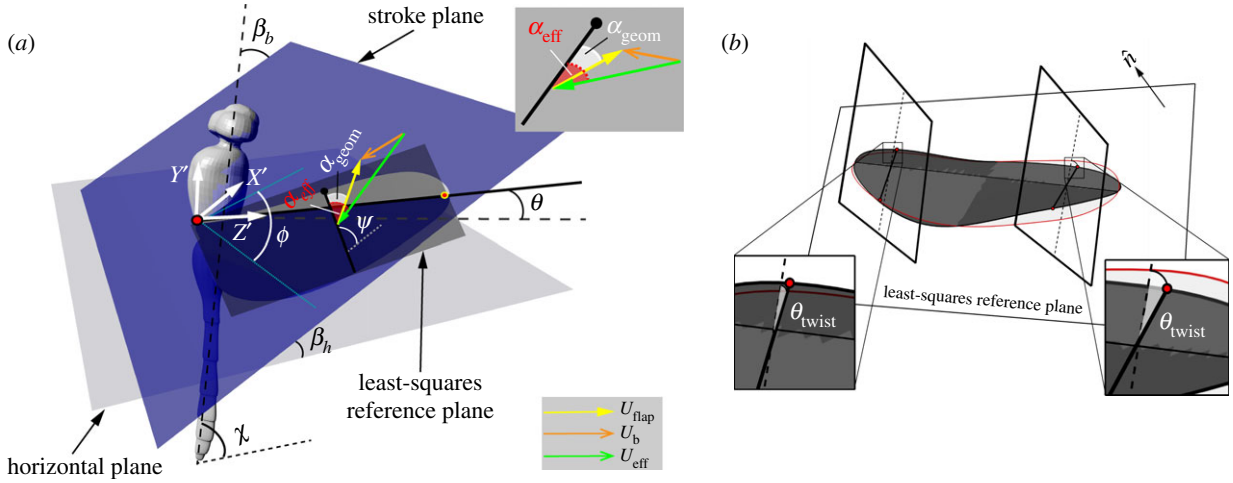

Figure 1. Kinematics definitions. (*a*) β_h and β_b are the stroke plane angles with respect to the horizontal and body longitudinal axis, respectively. ϕ, θ and ψ are the flap, deviation and pitch angles. U_{eff} is the vector sum of the wing (U_{flap}) and body (U_b) velocity. α_{eff} and α_{geom} are the effective and geometric angles of attack. χ is the body angle. (*b*) Twist angle (θ_{twist}). The deformed wing is shown in dark grey, and the least deformed wing is shown in light grey with a red outline. Two-dimensional (2D) cross-sections show that the angle between the chord line of the least deformed wing (dashed line) and deformed wing (solid line with red tip) is the twist angle. (Online version in colour.)

the AoA at locations between the leading edge and quarter-chord or near the rotation axis of the wing [19,41]. However, in classical aerodynamics (extended lifting line theory), the three-quarter chord (both for steady and unsteady flow) is the point of choice for calculating the AoA with respect to induced velocities for a wing in curved flow (Pistolesi's theorem) [42,43]. The geometric AoA (α_{geom}) excludes the body velocity. A least-squares reference plane (LSRP) is generated based on the nodes on the reconstructed wing surface to quantify wing twist (see [40]). The LSRP is a planar fitting to the 3D positions of the wing surface points where the sum of the distances of the wing surface points from this plane is minimized. The twist angle is the relative angle of the deformed wing chord line and the LSRP. These definitions are rendered in figure 1.

2.3. Computational fluid dynamics simulation

We used an in-house immersed boundary method flow solver for simulating incompressible flows in this study. We solved the incompressible Navier–Stokes equation (equation (2.1)) using a finite difference method with second-order accuracy in space and a second-order fractional step method for time stepping. More details of this approach and application can be found in other works [20,39,44,45]. Validations of the flow solver are in the works of Wan *et al*. [39] and Li & Dong [46].

$$\nabla \cdot \boldsymbol{u} = 0; \quad \frac{\partial \boldsymbol{u}}{\partial t} + \boldsymbol{u} \cdot \nabla \boldsymbol{u} = -\frac{1}{\rho}\nabla p + \upsilon \nabla^2 \boldsymbol{u}, \tag{2.1}$$

where $\boldsymbol{u}$ is the velocity vector in Cartesian coordinates, t the time, ρ the density, p the pressure and υ the kinematic viscosity.

The vortex structures are visualized by the λ_2-criterion [47], which has been used in previous insect flight studies [44,48]. The λ_2-criterion is based on the observation that a pressure minimum as a detection criterion is insufficient for locating vortex cores. Jeong & Hussain [47] opined that unsteady straining could cause a pressure minimum without vortical motion and viscous effects could also eliminate the pressure minimum in the flow when there is vortical motion. Hence, unsteady straining and viscous effect need to be eliminated to identify a vortex core properly.

The symmetric part of the gradient of equation (2.1) is expressed as

$$\mathbf{S}^2 + \Omega^2 = -\frac{1}{\rho}\nabla(\nabla p), \tag{2.2}$$

where $\boldsymbol{S} = 1/2[\nabla \boldsymbol{u} + (\nabla \boldsymbol{u})^{\mathrm{T}}]$ and $\boldsymbol{\Omega} = 1/2[\nabla \boldsymbol{u} - (\nabla \boldsymbol{u})^{\mathrm{T}}]$ are the strain rate and vorticity tensors, respectively, after the unsteady straining ($\mathrm{D}S/\mathrm{D}t$ term) and viscous effects (υ term) have been discarded. A vortex core is then defined as a region connected by real negative eigenvalues ($\lambda_2 < 0$) of equation (2.2).

We ran the simulations on a non-uniform Cartesian grid. The domain size was $50\bar{c} \times 50\bar{c} \times 50\bar{c}$ totalling 14 million grids. High-resolution uniform grids surround the insect in a volume of $13\bar{c} \times 15\bar{c} \times 23\bar{c}$ with a spacing of about $0.06\bar{c}$ with stretching grids extending from the fine region to the outer boundaries. The pressure and velocity boundary conditions at the domain's boundaries are homogeneous Neumann conditions set to zero. The Reynolds number defined by $\mathrm{Re} = \bar{U}_{tip}\bar{c}/\upsilon$ is about 1840, based on the average effective wing tip speed of the wing pair

$$\begin{aligned}\overline{U}_{tip} &= \overline{|\boldsymbol{u}_{tip} + \boldsymbol{u}_{body}|} \\ &= \frac{1}{T}\int_0^T \sqrt{(\dot{x}_{tip} + \dot{x}_{body})^2 + (\dot{y}_{tip} + \dot{y}_{body})^2 + (\dot{z}_{tip} + \dot{z}_{body})^2}\,\mathrm{d}t \\ &= 3.44\,\mathrm{m\,s^{-1}},\end{aligned}$$

where $\boldsymbol{u} = \langle \dot{x}, \dot{y}, \dot{z} \rangle$ is the time derivative of the displacement vector and T the flapping duration, mean-chord length ($\bar{c} = 0.008$ m), kinematic viscosity of air at room temperature ($\upsilon = 1.5 \times 10^{-5}\,\mathrm{m^2\,s^{-1}}$). Figure 2 shows the comparison of forces during the second stroke from three grid set-ups (coarse, medium and fine). The difference of both the mean and peak values between the medium-grid (adopted in this paper) and the fine-grid is about 2% (table 2) which indicates grid convergence following Liu *et al*.'s work [44].

3. Results

3.1. Kinematics

3.1.1. Body kinematics

The body kinematics are documented in figure 3. At the onset of flight, the dragonfly rested on a platform posing at an initial body angle of approximately 87°. There was a preparatory stage ($t = -20$ ms to 0 s). However, obvious body translation did not occur until the successive DS during which the wing generated enough propulsive force. This time instant ($t = 0$ s) is the start of the flight. The insect left the platform smoothly while increasingly leaning backward. Both the body velocity and angle increased for the next 2.5 flapping cycles slightly attenuating in the last half wingbeat. The centre of mass of

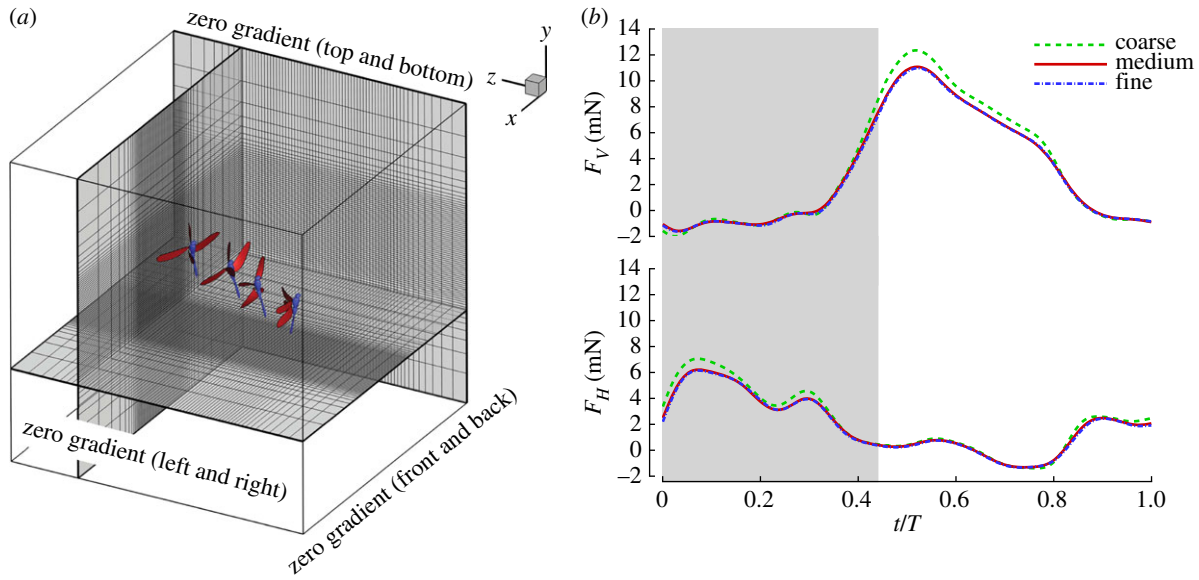

Figure 2. Computational set-up. (*a*) Computational mesh employed in the study. For display, the meshes coarsened four times. (*b*) Grid-independent study. The sum of the FW and HW forces is shown during the second stroke (F_v, vertical force; F_H, horizontal force). Grey shading indicates the FW DS. Medium grids are shown in (*a*). (Online version in colour.)

Table 2. Forces from three different grids set-up.

	grids	mean vertical force (mN)	max vertical force (mN)	mean horizontal force (mN)	max horizontal force (mN)
coarse	214 × 214 × 214	3.40	12.35	2.17	7.06
medium	240 × 240 × 240	3.08	11.08	1.93	6.22
fine	252 × 252 × 252	3.02	10.95	1.88	6.14

the body was elevated by about $5\bar{c}$ during the last two flapping cycles with most of the body motion occurring in the horizontal direction ($12\bar{c}$).

The average body angle during the entire flight duration was approximately 90°. The wings propelled the body backward with an average velocity of $-1\ \mathrm{m\,s^{-1}}$. The advance ratio (J), defined as the ratio of the average body to wingtip velocity is -0.31 ± 0.12. Because the dragonfly is accelerating, the advance ratio changes on a half stroke basis and is larger in the second and third flapping strokes. In addition to body motion, we observed some tail movement typical of dragonfly flight. The tail motion trailed the body's by about half a wingbeat, although the profile of the time histories was similar. At the beginning of the third US, the insect slowed down and reduced its body and tail angle (figure 3*e*,*f*).

3.1.2. Wing kinematics and deformations

Both wing pairs swept through a stroke plane (β_b) that maintained an orientation of $35 \pm 4°$ measured relative to the straight line that connects the head to the tail in the absence of body deformation (body longitudinal axis, figure 3*e*). This β_b is slightly less than the stroke plane angle measured in forward flight (relative to the longitudinal axis), which is about 50–60° [37,49]. Nevertheless, in the global frame, the stroke plane in backward flight is almost perpendicular to that in forward flight due to the change in the body angle in backward flight (figure 3*g*). The mean stroke plane angle relative to the horizon (β_h) is $46.8 \pm 5.5°$ for the FW and hindwings (HW).

Figure 4 shows the measured wing kinematics. The HW led the FW typical of dragonfly flight [49,50]. The phase difference increased from one stroke to another; approximately 37°, 51° and 94° for the three strokes, respectively. The phasing of the FW and HW may help reduce oscillations in the body posture during flight [31]. The DS-to-US duration ratio changed on a stroke-by-stroke basis from 0.9 (first stroke) to 0.7 (second stroke) to 1 (third stroke) for the FW and from 0.9 (first stroke) to 0.8 (second and third strokes) for the HW.

The wings flapped at high angles of attack while deforming considerably. We report the AoAs at four spanwise locations approximately 0.25, 0.5, 0.75 and 0.9R, where R is the distance from the wing root to tip (figure 4). The AoA decreased from root to tip. In the text, the mid-span (0.5R) AoA is reported. Averaged across all strokes, the DS α_{geom} was $39.0 \pm 2.2°$ and $47.0 \pm 3.7°$, and that for the US was $52.4 \pm 7.8°$ and $55.8 \pm 2.2°$ for FW and HW, respectively. Taking into account the body motion, we found that α_{geom} was significantly reduced. Hence, the DS α_{eff} was $22.5 \pm 2.1°$ and $26.1 \pm 9.3°$, and that for the US was $25.3 \pm 5.6°$ and $31.2 \pm 6.6°$ for the FW and HW, respectively. At these intermediate angles of attack, insect wings usually carry a stable LEV [1,51]. We also tracked the velocity of the leading edge at the spanwise locations where we calculated the angles of attack (see electronic supplementary material). Overall, the resultant wing velocities squared were higher during the US than the DS by 20 and 15% for the FW and HW at mid-span.

In addition to the rigid wing kinematics, the wing twist is reported in figure 4. The twist angle, which is the relative

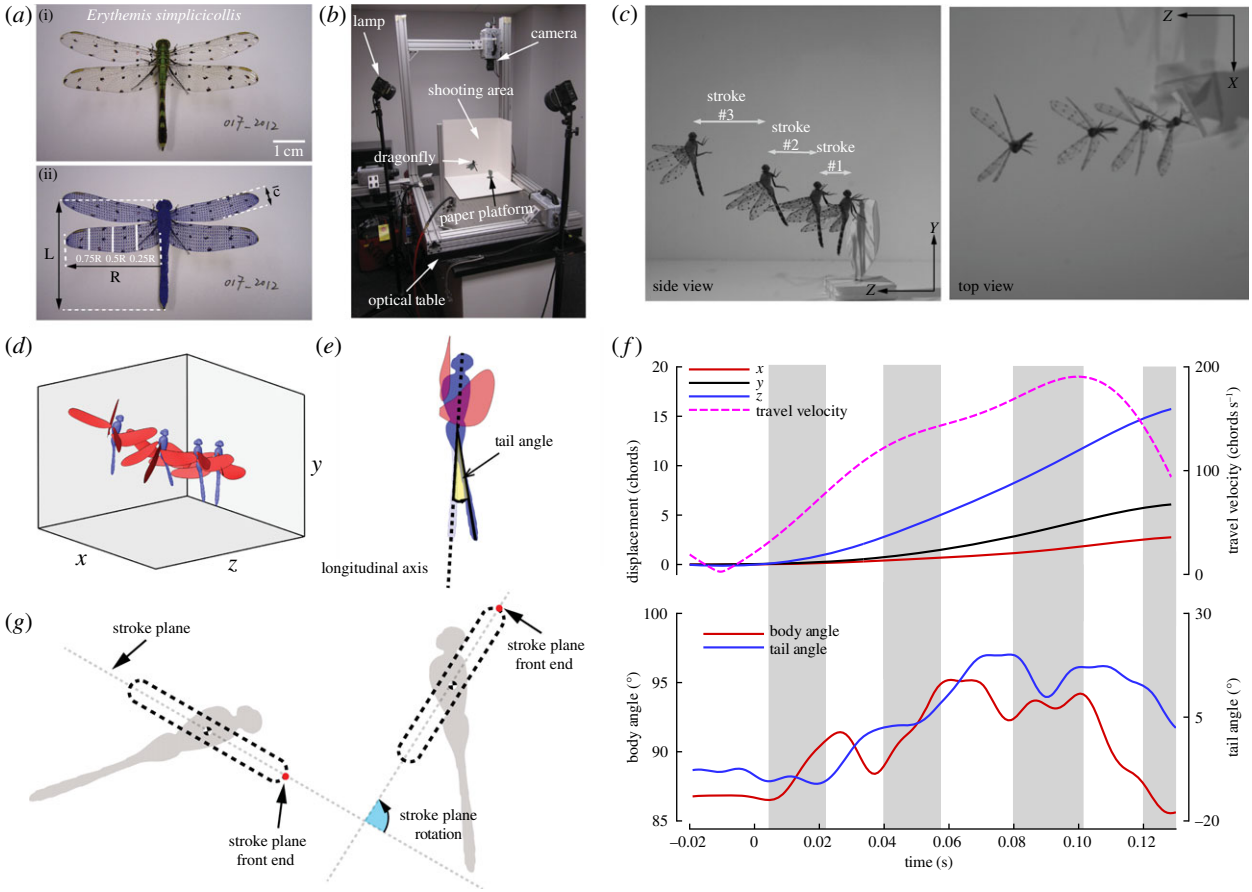

Figure 3. Body motion during backward flight. (*a*) Reconstructed dragonfly (ii) overlapped on a real image (i). *L*, body length; *R*, wing length from root to tip, $\bar{c}$, mean chord length. (*b*) Experimental set-up. (*c*) Snapshots of the dragonfly in backward flight. (*d*) Montage of 3D model of dragonfly used in CFD simulation. (*e*) Tail angle definition. The tail angle is the angle between the thorax and the tail. (*f*) Body kinematics. Grey shading denotes the FW DS. (*g*) Stroke plane reorientation (blue shading) due to change in body angle from forward to backward flight. (Online version in colour.)

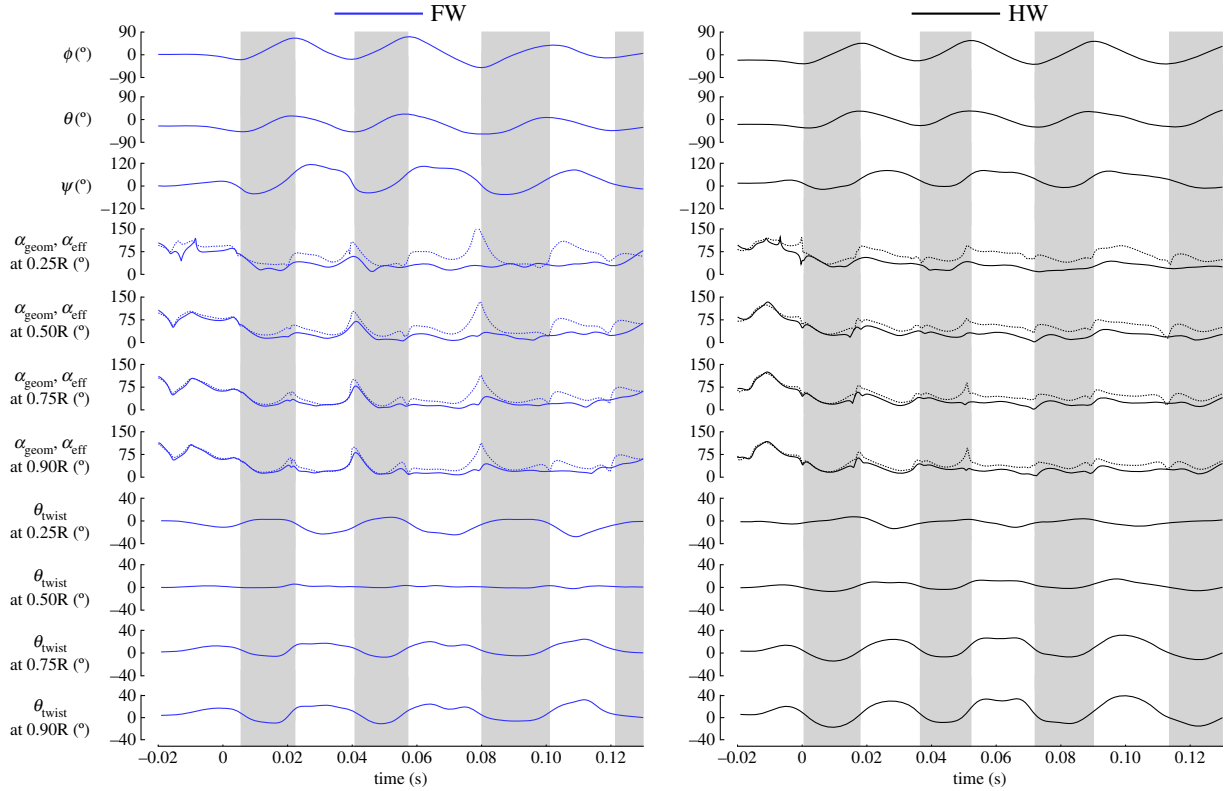

Figure 4. Wing kinematics and twist. The average Euler angles are shown. The geometric (dashed lines) and effective angles of attack (solid lines) and twist angles at four spanwise location are reported. Grey shading denotes the DS phase. (Online version in colour.)

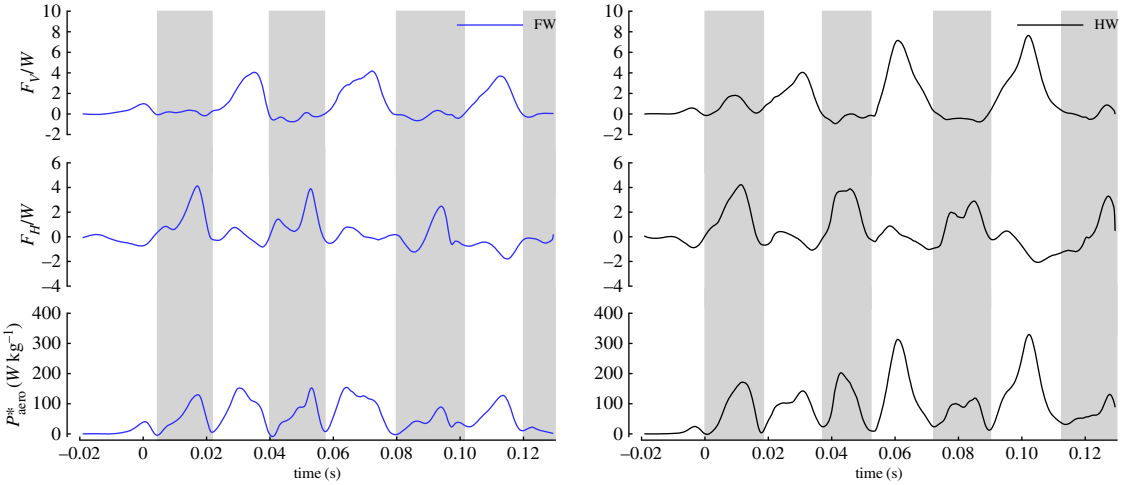

Figure 5. Force generation and muscle-specific power consumption. Time history of forces (F_v, vertical force; F_H, horizontal force; W, weight = 1.275 mN) and muscle-mass-specific power $(P*_{aero})$ consumption. Grey shading denotes the DS phase. (Online version in colour.)

angle of the deformed wing chord line and the LSRP (figure 1*b*), increased from mid-span to tip and is greater for the HW and during the US. The twist was as much as 40°, twice higher than previous measurements on dragonflies [40].

3.2. Force generation: aerodynamic force and power

The flight forces were computed by the integration of the wing surface pressure and shear stress. The aerodynamic power is defined as $p_{aero} = -\iint (\bar{\sigma} \cdot \bar{n})\bar{u}\, ds$, where $\bar{\sigma}$ is the stress tensor, $\bar{u}$ the velocity of the fluid adjacent to the wing surface, $\bar{n}$ and ds are the unit normal direction and the area of each element, respectively. The forces and muscle-mass-specific power consumption $(p*_{aero} = p_{aero}/M_m)$ are displayed in figure 5. The muscle mass (M_m) is 49% of the body mass based on previous measurements [52,53].

Consistent with the phase difference between the wing pairs, the peak forces produced by the HW led the FW. The magnitudes of peak vertical force generated by the FW (all USs) and HW (first DS) are similar (approx. 4 mN), while the peak vertical force of the HW is about twice FW in the second and third strokes as the insect ascends (see §3.1.1). The peak horizontal forces for the wing pairs are also comparable, although on average the HW generate greater horizontal forces.

Most of the vertical force is generated during the US, while horizontal force is generated in the DS. Both wing pairs generate larger forces in US compared to DS. Greater forces are produced by HW compared to FW. The peak vertical and horizontal forces during the flight are about 9 and 5.5 times the body weight, respectively. The dragonfly generates an average vertical force 2.5–3 times the body weight to sustain flight and ascend while propelling backward with an average force of 1.5 times the body weight.

The average muscle-mass-specific power consumed by the dragonfly was 146 W kg^{-1} (FW: 54 W kg^{-1}; HW: 92 W kg^{-1}). This was in the same range (76–156 and 160 W kg^{-1}) measured by Wakeling & Ellington [52] and Azuma *et al*. [50], respectively, for forward flight.

3.3. Force vectoring

Force vectoring is a mechanism commonly used by insects and birds to change flight direction. Using this strategy, body rotation is used to redirect the flight forces, especially if the forces are directionally constrained within the animal's body frame [33,36]. By rotating the body relative to the ground, the insect changes the global orientation of the aerodynamic force to perform the desired manoeuvre.

To investigate how the dragonfly's body posture affects the orientation of aerodynamic force vector, we visualized the half stroke-averaged force vectors in figure 6 in the Y–Z-plane which coincides with the mid-sagittal plane of the dragonfly. In figure 6*c*, the green and red arrows represent the DS-averaged $(\overline{F}_{DS})$ and US-averaged force vectors $(\overline{F}_{US})$, respectively. Although the magnitude of both US and DS forces change from cycle to cycle, $\overline{F}_{DS}$ and $\overline{F}_{US}$ were produced in a somewhat uniform direction with respect to the longitudinal axis of the body. The angle between the force vector and longitudinal axis is obtained from the dot product of the force vector and a unit vector parallel to the longitudinal axis. The angle between $\overline{F}_{US}$ and the longitudinal axis was 12 ± 8° (FW) and 10 ± 5° (HW). $\overline{F}_{DS}$ was oriented at 107 ± 15° (FW) and 96 + 18° (HW). The body posture tilted the DS force backward and the US force upward for generation of propulsive and lifting force, respectively. However, the change in magnitude of the force, as well as production of large aerodynamic forces in US, cannot be explained by force vectoring alone.

3.4. Vortical structures during backward flight: three-dimensional flow structures and leading edge vortex circulation

We plotted the iso-surface of the λ_2-criterion at two different values ($|\lambda_2| = 10, 15$) to visualize the flow structures (see electronic supplementary material for CFD simulation video). In figure 7, we present the evolution of the wake structures during the second stroke based on the HW timing. Whereas in figure 8, the flow structures are shown during maximum force production. The flow features on the right wings are reported, although the flow phenomena are similar on both sides of the wings.

An LEV forms as the wings translate during the DS. For most of the stroke (figure 7), the LEV grows in size and strength while being stably attached. During the DS, an LEV and TV are observed, and the vorticity in the LEV feeds into a tip vortex (TV). As reversal approaches, the LEV deteriorates and sheds

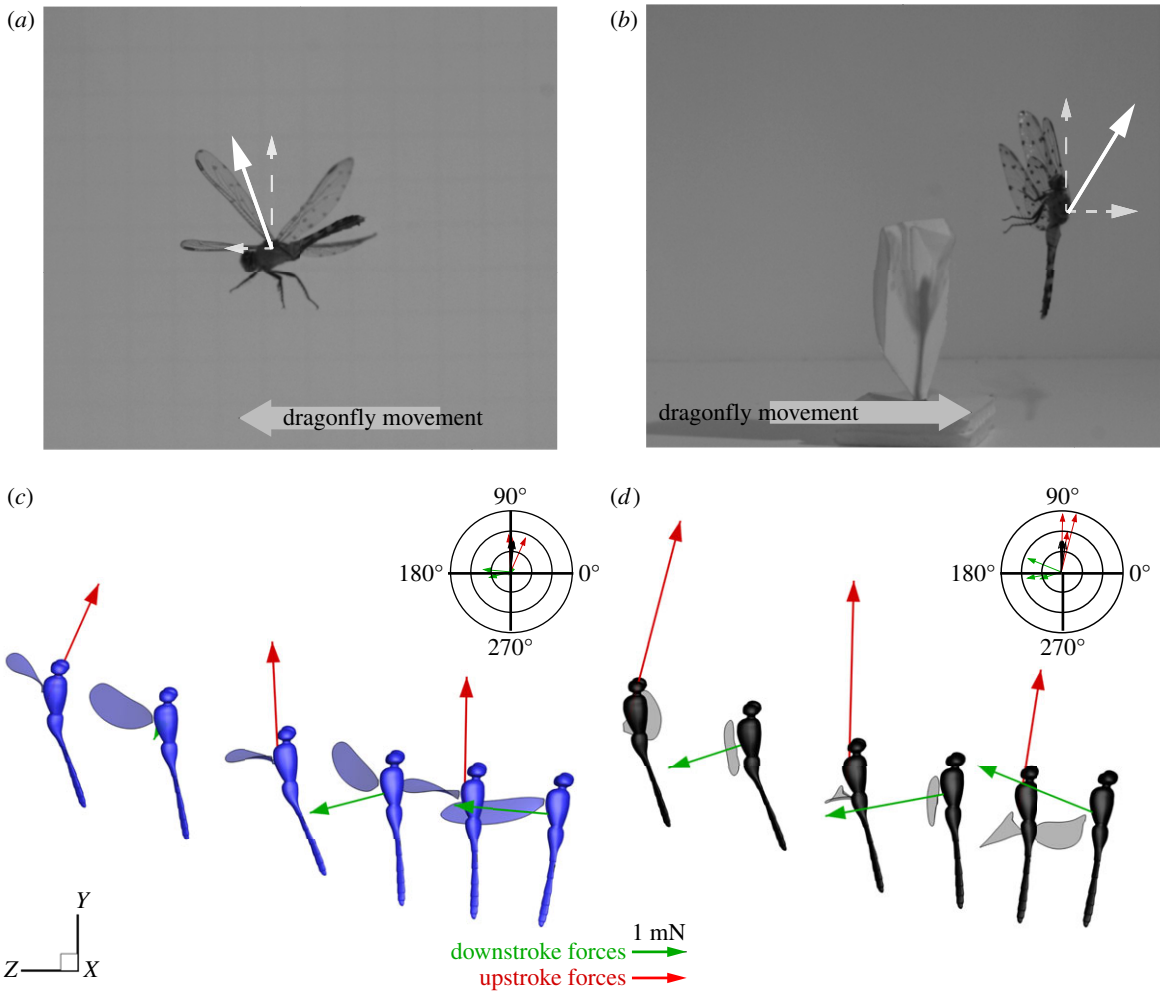

Figure 6. Force vectors in mid-sagittal plane. (*a*,*b*) Anecdotally using real footage, how dragonflies may appropriate the force vectoring for forward and backward flight. Solid and dashed arrows show resultant force and its components, respectively. (*c*,*d*) Measured flight forces. The dragonflies are coloured based on FW (blue) and HW (black) timing. Red and green force vectors represent $\overline{F}_{US}$ and $\overline{F}_{DS}$, respectively. In the polar plot, black vectors clustered around 90° indicate the body longitudinal axis. (Online version in colour.)

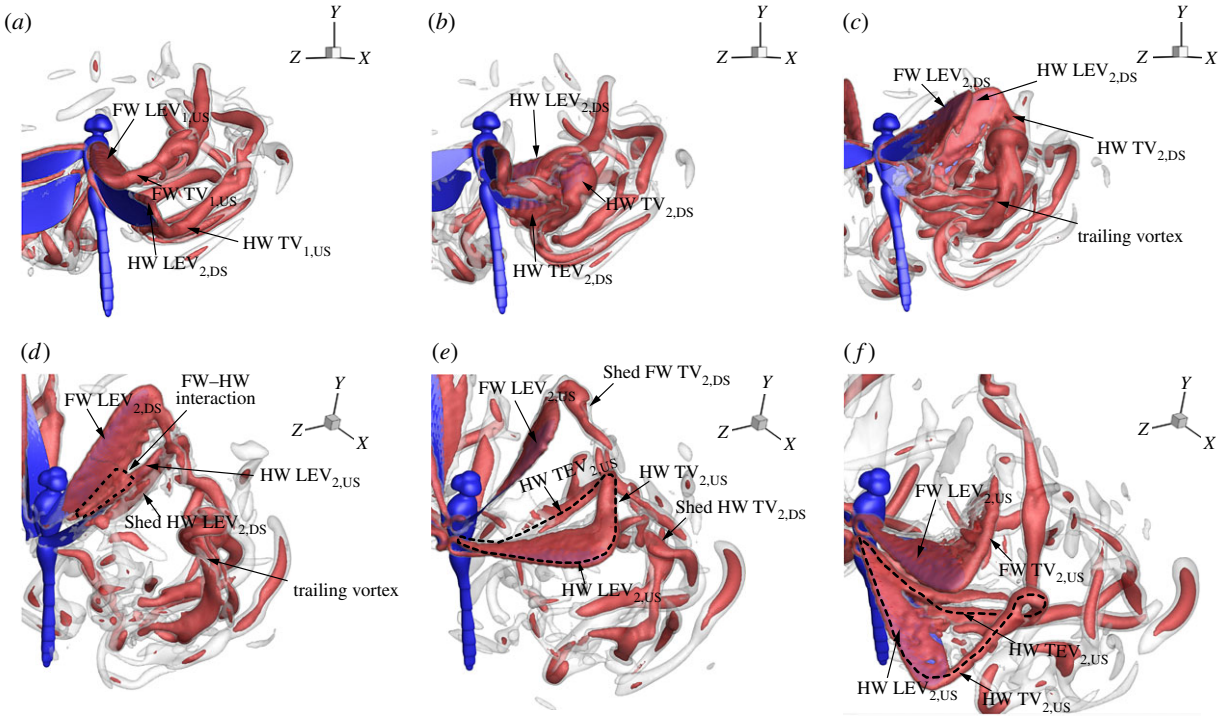

Figure 7. Vortex development in backward flight. The flow features visualized by the λ_2-criterion during the second flapping stroke. TEV, trailing edge vortex; TV, tip vortex. Subscripts 1, 2 denote vortices created by flapping strokes 1 and 2. Top row (*a*–*c*) represents snapshots during HW DS at $t/T = 0.07$, 0.19 and 0.34, respectively. The bottom row (*d*–*f*) represents snapshots during HW US at $t/T = 0.52$, 0.70 and 0.87, respectively. (Online version in colour.)

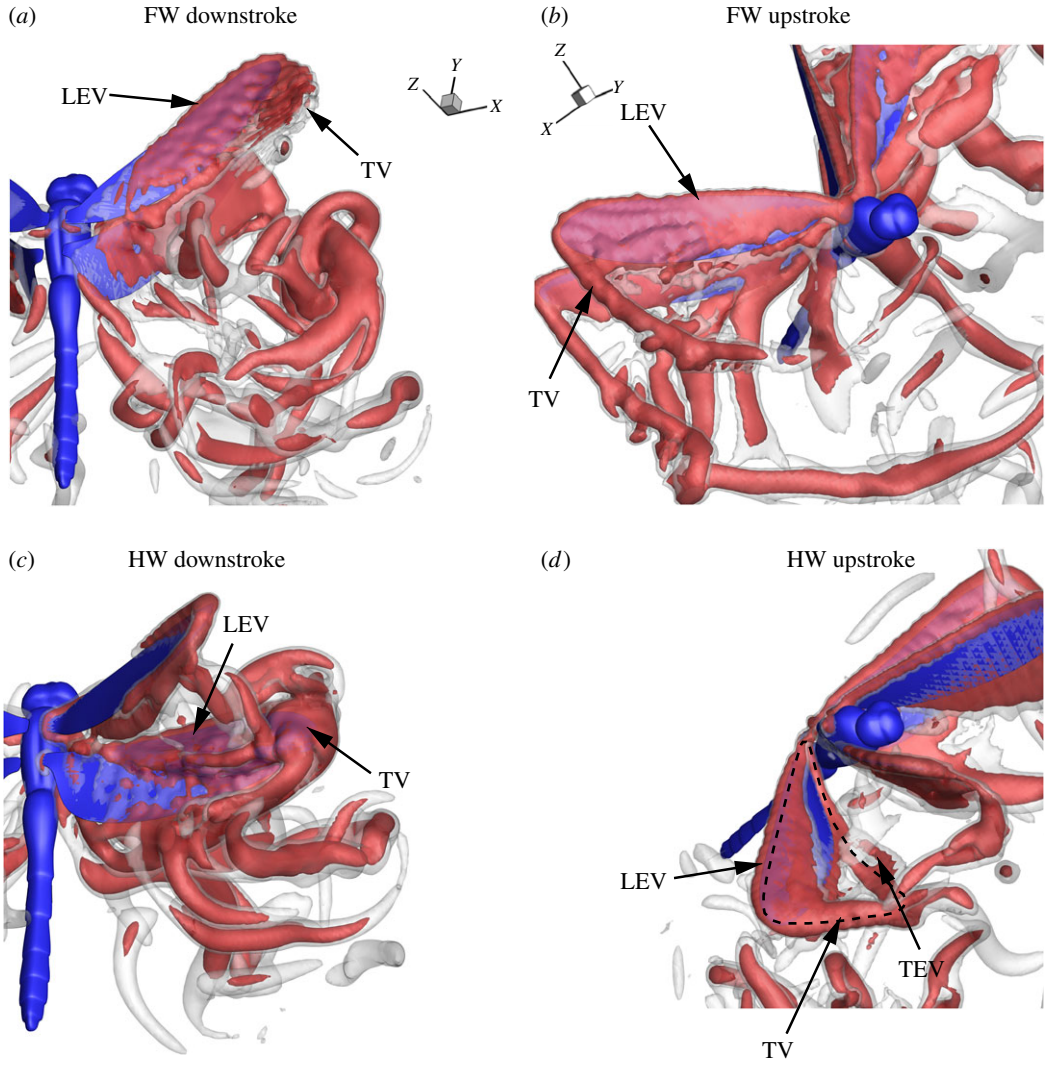

Figure 8. Flow features at maximum force production during second stroke for each wing pair. (*a*) FW DS $t/T = 0.35$, (*b*) FW US $t/T = 0.82$, (*c*) HW DS $t/T = 0.25$, (*d*) HW US $t/T = 0.70$. (Online version in colour.)

from the trailing edge. Concurrently, another vortex forms on the upper surface of the wing during reversal because of the rapid increase in AoA during wing rotation (figure 7*d*).

In the US, the LEV formed covers the entirety of the wing surface (figures 7*e*,*f* and 8*b*,*d*). The LEV in the US is larger than that formed in the DS. The TV is also more pronounced and suggests that the strength of the LEV feeding it may be greater than the DS's. Also, both the FW and HW have LEVs on them. During the mid-US and at maximum force production, the HW flow consists of an LEV, TV and a trailing edge vortex (TEV) connected to form a vortex loop (figures 7*e* and 8*d*). The loop creates a downward jet which boosts vertical force production.

We also quantified the strength (circulation) of the LEV throughout the second and third stroke. At every time step, a 2D plane normal to the axis of LEV was constructed (figure 9*a*). A vorticity threshold was set to capture the vortex. The circulation is the flux of the vorticity and is non-dimensionalized by the product of a reference velocity, U_{ref}, and length, l (equation (3.1)).

$$\Gamma^{*}_{\mathrm{LEV}} = \frac{1}{lU_{\mathrm{ref}}} \iint_{S} \omega \cdot \mathrm{d}S, \tag{3.1}$$

where ω is the vorticity. The area of integration ($\mathrm{d}S$) is bound by the vorticity threshold. $\bar{U}_{\mathrm{tip}}$ and $\bar{c}$ were chosen for the non-dimensionalization. The instantaneous LEV circulation at mid-span ($0.5R$) is displayed in figure 9*c*. There is a discontinuity at reversal due to the deterioration of the LEV and the emergence of another LEV on the opposite surface of the wing. The circulation slightly lags behind the kinematics due to the delay of growth of circulation in the vortex formation process during wing excursion.

The peak circulation (figure 9*c*) occurs in the same region where maximum force is generated for each wing pair (figure 5). The HW have higher LEV circulation than the FW. Also, the LEV circulation in the US is greater than the DS's. All the DS-to-US LEV circulation ratios are less than unity (table 3). The spanwise distribution of circulation on the wing surface at the instant of maximum force production in the second and third stroke are reported in figure 9*d*,*e*. The circulation increases along the span and tapers towards the tip. The US circulation, shown in dashed lines, is higher than the DS circulation, consistent with greater flight force generated in the US.

3.5. Wing–wing interaction

We observed some interaction between the wings during backward flight (figure 7*d*). Previous studies have indicated that the FW experience in-wash due to the HW and the HW are affected by the downwash from the FW with benefits

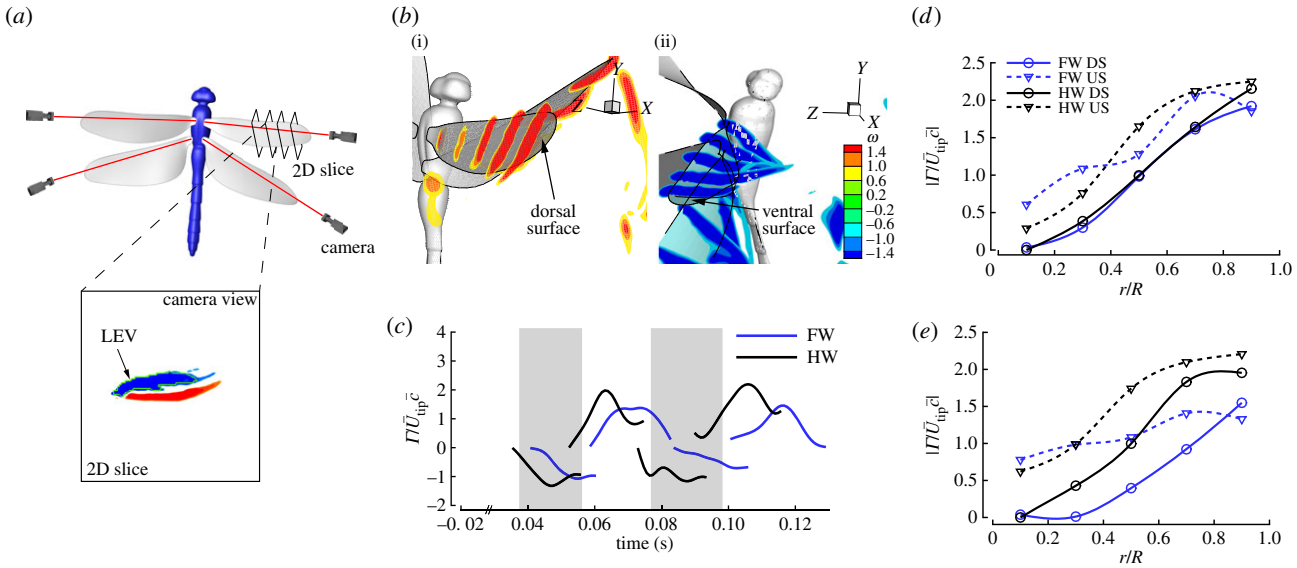

Figure 9. LEV circulation. (*a*) Schematic of a dragonfly with 2D slices on the wings with the virtual camera looking through a line passing through the LEV core. (*b*) Spanwise vorticity on FW during the (i) DS (dorsal surface shaded in grey) and (ii) US in the third stroke (ventral surface shaded in blue). (*c*) LEV circulation during the second and third stroke. Grey shading denotes FW DS. (*d*,*e*) Spanwise distribution of LEV circulation at maximum force production during the second and third stroke, respectively. (Online version in colour.)

Table 3. Quantification of LEV circulation. $\bar{\Gamma}^*$ represents the time half stroke averaged values. $\bar{\Gamma}^*_{\max}$ represents the maximum circulation per half stroke. All values are measured at 0.50*R*.

flapping stroke			$\bar{\Gamma}^*$	$\bar{\Gamma}^*_{\max}$	$\lvert\bar{\Gamma}^*_{DS}/\bar{\Gamma}^*_{US}\rvert$	$\lvert\Gamma^*_{\max_{DS}}/\Gamma^*_{\max_{US}}\rvert$
second	FW	DS	−0.67	−1.08	0.64	0.81
		US	1.05	1.34		
	HW	DS	−0.96	−1.32	0.83	0.67
		US	1.16	1.98		
third	FW	DS	−0.35	−0.71	0.40	0.49
		US	0.88	1.45		
	HW	DS	−0.89	−1.16	0.59	0.53
		US	1.50	2.19		

Table 4. Effect of WWI during flight (all strokes combined).

	forewings		hindwings	
force (10^{-3} N)	FO	ALL	HO	ALL
vertical force during entire duration	1.26	1.37 (8.7% ↑)	2.17	2.27 (4.6% ↑)
horizontal force during entire duration	0.63	0.52 (17.5% ↓)	0.68	0.77 (13.2% ↑)
vertical force during US	2.49	2.75 (10.4% ↑)	3.98	4.13 (3.77% ↑)
horizontal force during DS	1.28	1.21 (5.5% ↓)	2.16	2.18 (0.9% ↑)

being dependent on the phase difference between wing pairs [31,54–57]. Experiments on hovering kinematics showed that both wing pairs generate maximum lift when the HW lead by a quarter of the cycle and the distance between the wings is closest [54]. By leading the FW, the HW avoids the FW's downwash. Simulations of dragonfly-like wings at different advance ratios and phase differences indicated that total forces of the FW and HW are influenced by wing–wing interaction (WWI) when the HW lead the FW [56]. Lehmann [58] reported that an HW leading by 90° could achieve the same mean lift as an isolated wing due to wake capture. The FW could also benefit from interaction due to the distortion of the FW wakes by the HW via the 'wall effect' [20,58,59].

We compared three simulation cases: (i) with all four wings (ALL; shown in figures 8 and 9), (ii) the FW only (FO), and (iii) HW only (HO), to elucidate WWI during flight (table 4).

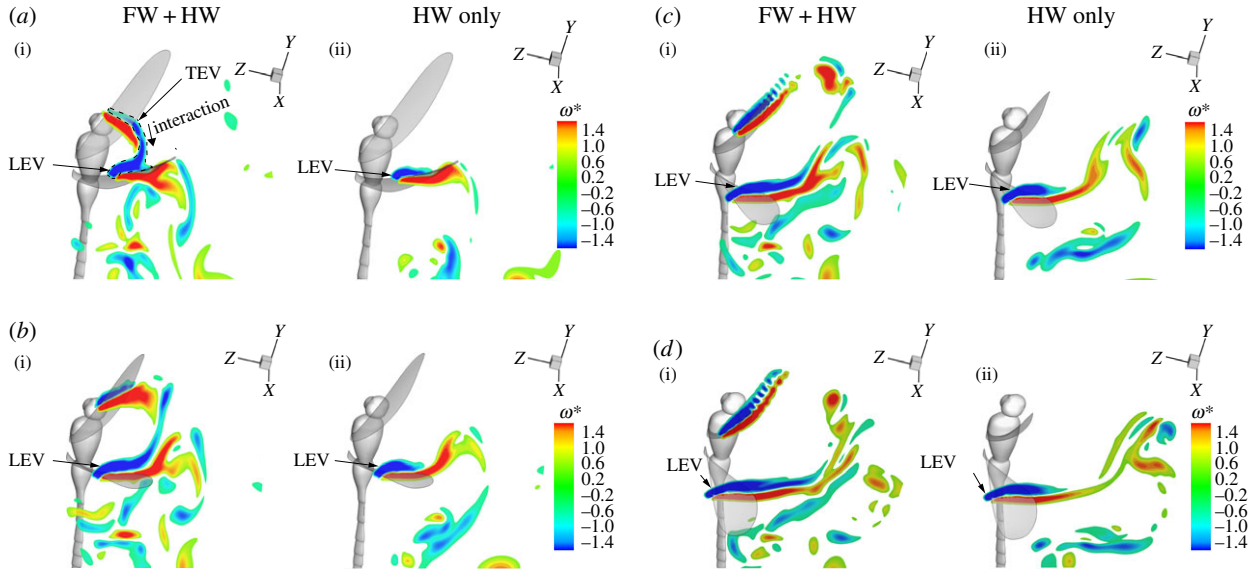

Figure 10. Visualization of vortical structures at mid-span during WWI. Slices similar to figure 9*a*,*b* are shown here to elucidate WWI. A–D represent snapshots where WWI occurred as labelled in figure 12. The region of interaction is shown in dashed lines with an arrow indicating the direction of vorticity transfer (*a* (i)). Contours represent non-dimensional vorticity. (Online version in colour.)

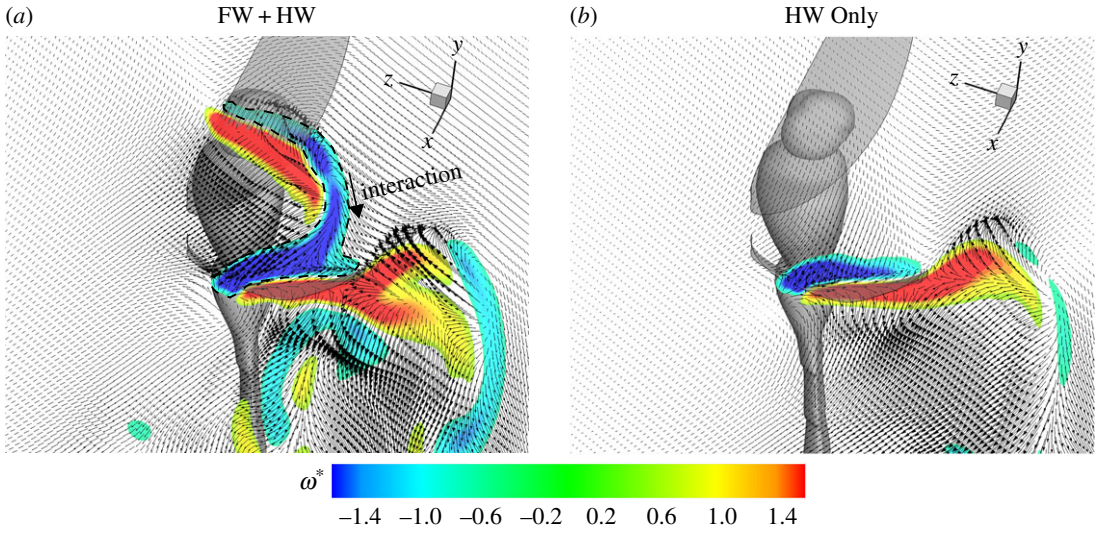

Figure 11. Mechanism of WWI. This figure shows the mechanism of vorticity transfer from the fore to HW during backward flight. (Online version in colour.)

On average, both wing pairs benefited from WWI for vertical force production. The FW and HW vertical forces were boosted by 8.7 and 4.6%, respectively. For thrust production, the interaction was detrimental for the FW leading to a 17.5% decrease in force while benefiting the HW by as much as 13.2%. During the US, both pairs of wings profited from WWI; 10.4% and 3.7% for the FW and HW, respectively. During the DS, horizontal forces for the FW are attenuated by 5.5%.

The mechanism of WWI which led to increased force production during the second stroke is shown in figures 10 and 11. In figure 10, the vortical structures are projected on a 2D slice cut at mid-span, similar to figure 9*a*. At the onset of interaction, vorticity emanating from the FW's trailing edge feeds into an already stronger LEV on the HW, boosting its circulation (figure 10*a*(i)). As the wings separate from each other during the excursion, the initial increase in HW LEV circulation is maintained in addition to the new vorticity influx formed as the LEV grows during translation (figure 10*b*–*d*). Comparing this finding to the HW only case, there is no vorticity transfer from the FW and the LEV is smaller.

In figure 11, the velocity field is superimposed on the vorticity contours in a zoomed in a snapshot of figure 10*a*. The FW TEV and HW LEV are linked together due to interaction (figure 11*a*). The presence of the FW induces an additional inflow into the LEV which is favourable in this case. This influx is absent in the HW only case, leading to the formation of a weaker LEV and consequently, a weaker jet below the wing (figure 11*b*).

4. Discussion and conclusion

Alterations in kinematics and aerodynamic features which are different from hovering and forward flight characterize backward flight of dragonflies. Our study shows that dragonflies can use backward flight as an alternative to forward flight voluntarily. Backward flight is not merely a transient behaviour but is sustainable for a relatively extended period, which may have implications for biology (prey capture or predator evasion) as well as MAV design. To fly backward, dragonflies tilt

Table 5. Kinematic parameters of several organisms in flight.

flight mode	Re	J	phase shift (°)	stroke plane (°)		body angle (°)	angle of attack (°)			
				β_{FW}	β_{HW}	χ	α_{FW}^{down}	α_{FW}^{up}	α_{HW}^{down}	α_{HW}^{up}
dragonfly										
hovering[a] [31]	4232	0	22	53	44	14	83	10	87	15
hovering [60,61]	1350	0	180	52	52	—	—	—	—	—
forward [62]	3100	0.30	60	52	52	—	50	15	50	15
forward[a] [51,63]	1100	0.75	—	—	25	—	—	—	25	15
forward ascending [50]	3200	0.13	77	37	40	10	24.1	11.8	27	22.9
forward [37]	—	0.21–0.47	47–110	9–28	7–29	23–36	—	—	—	—
backward (current)	1840	−0.30	37–94	47	47	85–95	21	32	37	55
hummingbird										
backward [13]	—	−0.30	—	0–6		50–75	—	—	—	—
waterlily beetle										
backward [38]	—	—	—	0–30		50–70	—	—	—	—
Delfly II										
backward [16]	—	—	—	—		70–100	—	—	—	—

[a]Tethered.

α is the instantaneous geometric angle of attack at midstroke.

Table 6. Force asymmetry: DS versus US. This table reports the contribution of each half stroke to the total aerodynamic force during a flapping cycle in different flight modes of insects.

insect	flight mode	DS force (%)	US force (%)	reference
cicada	forward	80	20	Wan *et al*. [39]
damselfly	forward	75	25	Sato *et al*. [6]
		84	16	Bode-Oke *et al*. [20]
	take-off	50	50	
dragonfly	backward	33	67	current study
	forward	80	20	Azuma & Watanabe [49]
bumblebee	forward	50–100		Dudley [64]
fruit fly	hovering	37	63	Fry *et al*. [3]
	saccade	40	60	Fry *et al*. [2]
	forward	61	39	Meng & Sun [65]
hawkmoth	forward	80	20	Willmott *et al*. [66]
mosquito	hovering	43	57	Bomphrey *et al*. [67]
honeybee	hovering	43	57	Altshuler *et al*. [18]

their stroke plane towards their bodies, but the primary reorientation of the stroke plane and force vector is because of the steep body posture that is maintained. In addition to redirecting the force, we found that the force magnitude is significantly increased in the US (when compared with forward flight). In contrast with forward flight, during which dragonflies generates little force in US [49], the magnitude of the half-stroke-averaged force generated in US during backward flight is two to four times the body weight. In addition, we showed that a strong and stable LEV in the US was responsible for greater force production (figure 9 and table 3). The flow visualizations corroborated these findings in figures 7 and 8. The mechanism of WWI was also illustrated (figures 10 and 11). Vorticity from the FW trailing edge enhanced the HW's LEV.

Here, we compare our findings; kinematics, aerodynamics and flow features, with hovering and forward flights which have been documented in the literature. Tables 5 and 6 show a summary of previous research on different flight modes. The high body angles (χ) during dragonfly backward flight parallels similar observations of hummingbird [13] and insect

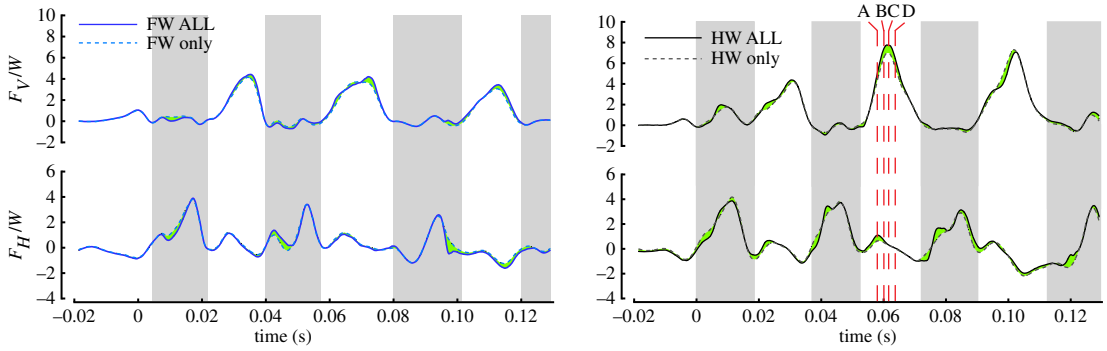

Figure 12. WWI. The solid lines and dashed lines indicate the ALL case and where the wings are isolated, respectively. The difference is shaded in green. A–D represent snapshots where the flow field is evaluated in figure 10. (Online version in colour.)

backward flight [11] and could be a mechanism of convergent evolution [13]. However, χ was significantly larger than those of hummingbirds (50–75°) which use a horizontal stroke plane and waterlily beetles (50–70°), which use an inclined stroke plane [13,38]. Our χ corroborated previous observation in dragonfly backward flight (100°) [11]. A state-of-the-art MAV, the Delfly-II, has also been shown to induce backward flight by increasing its body angle to about 100° from its stable flight configuration [16].

Although a steep body posture during backward flight has been thought to generate higher drag due to a higher projected area, Sapir & Dudley [13] showed that drag forces only differed by 3.6% between backward and forward flight in hummingbirds. It is not certain whether by maintaining a high body angle, dragonflies will drastically increase body drag because they possess slender bodies. While body drag is present, we measured it to be 11 times smaller than the horizontal forces being generated by the wings during flight. The steep body angle is in contrast with forward and hovering flight during which the dragonfly keeps its body slightly inclined from the horizontal (approx. 2–40°) [31,37,49]. We define the parasite drag (pressure drag + viscous drag on the body) coefficient as $C_D = \bar{F}_H/0.5\rho\bar{U}_b^2 S_{\text{frontal}}$, where $\bar{F}_H$ is the mean horizontal force and $\bar{U}_b$ the average translation velocity of the body and S_{frontal} the frontal area presented to the flow. Comparing the C_D measured from our simulation (Reynolds number based on body length, $\text{Re}_b \sim 3860$) with results for forward flight of dragonflies of similar Re_b approximately 2460–7790 in the literature, the results were comparable indicating that an upright body posture did not substantially influence body drag production. Our measured C_D was 0.57 and within the range (0.31–0.84) found in the literature [53,68].

During backward flight, the dragonfly wings swept through a stoke plane (β_b) inclined at $35 \pm 5°$; an angle shallower than β_b of dragonflies of similar mass and morphology in forward flight by 15° [37,50]. The stroke plane with respect to the horizon (β_h) during backward flight was reported as $46.8 \pm 5.5°$ for both wing pairs which also was about 20–40° greater. Compared to hovering [61], β_h in backward flight was about 15° less.

For force production, a strong LEV was present on both wing pairs. Contrary to previous works on dragonfly forward flight [1,30,62], the presence of the LEV was not limited to the FW but was evident on the HW as well [51]. The LEV was also present in both half strokes with the US LEV being stronger. We verified this finding by calculating the LEV circulation of the wing and found DS-to-US LEV circulation ratios as low as 0.4 and 0.59 for the FW and HW, respectively. In previous works, the LEV circulation was significantly larger in DS compared to US where the LEV may be completely absent [20,66,69–71]. Willmott *et al*. [66] noted that the US TV was relatively weak in comparison to the DS's. Hence, the LEV circulation should be much smaller than that measured in the DS. From their smoke visualization and analysis, there was no hint of an LEV to enhance lift in the US. Thomas *et al*. [1] also arrived at a similar conclusion with smoke visualizations on dragonflies in tethered and free forward light. Wang & Sun [62], using CFD, verified the absence of the LEV in the US in hovering as well as forward flight of dragonflies. The reason for LEV absence during the US was attributed to very low angles of attack as the wing slices through the air, hence, no flow separation. Higher angles of attack were recorded in our study (figure 4) and we observed the formation of a stable LEV on the wing surface (figures 7 and 8).

The higher LEV circulation and forces in the US shows that during backward flight, dragonflies use an aerodynamically active US (figures 5, 8 and 12). This is achieved by inducing large angles of attack plus an enhancement in velocity of the wing, resulting from the body's backward motion, in the US. Owing to their relatively low flapping frequency, the magnitude of body velocity of a dragonfly is comparable to its wing velocity. Thus, the motion of the body can yield significant effects on the net wing velocity. In contrast with backward flight, during forward and hovering flight, most of the flight force is produced in the DS [20,31,72]. In these flight modes, the DS is conventionally regarded as vertical force producing and the US, thrust (horizontal force) producing [11,31,50]. Also, the forces generated in the US are significantly less (inactive) and account for about 10–20% of the body weight [8,20,66]. Current literature, summarized in table 6, indicates that, during forward flight, the DS generates 80% of the total force created by cicadas [39], 80% for dragonflies [49], 75–84% for damselflies [6] and 80% of body weight in hawkmoths [66]. As flight speed increases, the relative contribution of the US in force production diminishes [8,20]. During backward flight, the US must become active because of its weight supporting role. Previously, there has been some evidence of the US producing larger forces than the DS such as hovering and saccadic flight of Drosophila (60–63%) [2,3], hovering flight of mosquitos (57%) [67] and honeybees (57%) [18]. However, in contrast with dragonflies, these insects use a horizontal stroke plane in the flight scenarios listed.

Data accessibility. This article has no additional data.

Authors' contributions. A.T.B.-O. carried out the 3D reconstructions and CFD simulation. All authors interpreted the data. A.T.B.-O. drafted the initial manuscript. All authors contributed to the final paper.

Competing interests. We declare we have no competing interests.

Funding. Funding support from National Science Foundation (CBET-1313217) and Air Force Office of Scientific Research (FA9550-12-1-007).

References

1. Thomas AL, Taylor GK, Srygley RB, Nudds RL, Bomphrey RJ. 2004 Dragonfly flight: free-flight and tethered flow visualizations reveal a diverse array of unsteady lift-generating mechanisms, controlled primarily via angle of attack. *J. Exp. Biol.* **207**, 4299–4323. (doi:10.1242/jeb.01262)
2. Fry SN, Sayaman R, Dickinson MH. 2003 The aerodynamics of free-flight maneuvers in *Drosophila*. *Science* **300**, 495–498. (doi:10.1126/science.1081944)
3. Fry SN, Sayaman R, Dickinson MH. 2005 The aerodynamics of hovering flight in *Drosophila*. *J. Exp. Biol.* **208**, 2303–2318. (doi:10.1242/jeb.01612)
4. Muijres FT, Elzinga MJ, Melis JM, Dickinson MH. 2014 Flies evade looming targets by executing rapid visually directed banked turns. *Science* **344**, 172–177. (doi:10.1126/science.1248955)
5. Dickinson MH, Muijres FT. 2016 The aerodynamics and control of free flight manoeuvres in *Drosophila*. *Phil. Trans. R. Soc. B* **371**, 20150388. (doi:10.1098/rstb.2015.0388)
6. Sato M, Azuma A. 1997 The flight performance of a damselfly *Ceriagrion melanurum Selys*. *J. Exp. Biol.* **200**, 1765–1779.
7. Phan HV, Nguyen QV, Truong QT, Van Truong T, Park HC, Goo NS, Byun D, Kim MJ. 2012 Stable vertical takeoff of an insect-mimicking flapping-wing system without guide implementing inherent pitching stability. *J. Bionic Eng.* **9**, 391–401. (doi:10.1016/S1672-6529(11)60134-0)
8. Ellington CP. 1999 The novel aerodynamics of insect flight: applications to micro-air vehicles. *J. Exp. Biol.* **202**, 3439–3448.
9. De Croon GCHE, Perçin M, Remes B. 2016 *The DelFly design, aerodynamics, and artificial intelligence of a flapping wing robot*. 1st edn. Amsterdam, the Netherlands: Springer.
10. Dickinson MH, Lehmann F-O, Sane SP. 1999 Wing rotation and the aerodynamic basis of insect flight. *Science* **284**, 1954–1960. (doi:10.1126/science.284.5422.1954)
11. Rüppell G. 1989 Kinematic analysis of symmetrical flight manoeuvres of Odonata. *J. Exp. Biol.* **144**, 13–42.
12. Rüppell G, Hilfert D. 1993 The flight of the relict dragonfly *Epiophlebia superstes* (Selys) in comparison with that of the modern Odonata (Anisozygoptera: Epiophlebiidae). *Odonatologica* **22**, 295–309.
13. Sapir N, Dudley R. 2012 Backward flight in hummingbirds employs unique kinematic adjustments and entails low metabolic cost. *J. Exp. Biol.* **215**, 3603–3611. (doi:10.1242/jeb.073114)
14. Yokoi T, Fujisaki K. 2009 Hesitation behaviour of hoverflies *Sphaerophoria* spp. to avoid ambush by crab spiders. *Naturwissenschaften* **96**, 195–200. (doi:10.1007/s00114-008-0459-8)
15. Zeil J, Wittmann D. 1989 Visually controlled station-keeping by hovering guard bees of *Trigona* (*Tetragonisca*) *angustula* (Apidae, Meliponinae). *J. Comp. Physiol. A* **165**, 711–718. (doi:10.1007/BF00611002)
16. Caetano JV, de Visser CC, Remes BD, De Wagter C, Van Kampen E-J, Mulder M. 2013 *Controlled flight maneuvers of a flapping wing micro air vehicle: a step towards the DelFly II Identification*. In *AIAA Atmospheric Flight Mechanics* (*AFM*) *Conference, Boston, MA, 19–22 August*, pp. 4843. Reston, VA: American Institute of Aeronautics.
17. Lehmann FO, Dickinson MH. 1998 The control of wing kinematics and flight forces in fruit flies (*Drosophila* spp.). *J. Exp. Biol.* **201**, 385–401.
18. Altshuler DL, Dickson WB, Vance JT, Roberts SP, Dickinson MH. 2005 Short-amplitude high-frequency wing strokes determine the aerodynamics of honeybee flight. *Proc. Natl Acad. Sci. USA* **102**, 18213–18218. (doi:10.1073/pnas.0506590102)
19. Chen MW, Zhang YL, Sun M. 2013 Wing and body motion and aerodynamic and leg forces during take-off in droneflies. *J. R. Soc. Interface* **10**, 20130808. (doi:10.1098/rsif.2013.0808)
20. Bode-Oke A, Zeyghami S, Dong H. 2017 Aerodynamics and flow features of a damselfly in takeoff flight. *Bioinspir. Biomim.* **12**, 056006. (doi:10.1088/1748-3190/aa7f52)
21. Lehmann FO, Dickinson MH. 1997 The changes in power requirements and muscle efficiency during elevated force production in the fruit fly *Drosophila melanogaster*. *J. Exp. Biol.* **200**, 1133–1143.
22. Lentink D, Dickinson MH. 2009 Rotational accelerations stabilize leading edge vortices on revolving fly wings. *J. Exp. Biol.* **212**, 2705–2719. (doi:10.1242/jeb.022269)
23. Birch JM, Dickson WB, Dickinson MH. 2004 Force production and flow structure of the leading edge vortex on flapping wings at high and low Reynolds numbers. *J. Exp. Biol.* **207**, 1063–1072. (doi:10.1242/jeb.00848)
24. Nabawy MRA, Crowther WJ. 2017 The role of the leading edge vortex in lift augmentation of steadily revolving wings: a change in perspective. *J. R. Soc. Interface* **14**, 20170159.
25. Shyy W, Liu H. 2007 Flapping wings and aerodynamic lift: the role of leading-edge vortices. *AIAA J.* **45**, 2817–2819. (doi:10.2514/1.33205)
26. Muijres F, Johansson L, Barfield R, Wolf M, Spedding G, Hedenström A. 2008 Leading-edge vortex improves lift in slow-flying bats. *Science* **319**, 1250–1253. (doi:10.1126/science.1153019)
27. Ristroph L, Bergou AJ, Guckenheimer J, Wang ZJ, Cohen I. 2011 Paddling mode of forward flight in insects. *Phys. Rev. Lett.* **106**, 178103. (doi:10.1103/PhysRevLett.106.178103)
28. Sane SP. 2003 The aerodynamics of insect flight. *J. Exp. Biol.* **206**, 4191–4208. (doi:10.1242/jeb.00663)
29. Chin DD, Lentink D. 2016 Flapping wing aerodynamics: from insects to vertebrates. *J. Exp. Biol.* **219**, 920–932. (doi:10.1242/jeb.042317)
30. Bomphrey RJ, Nakata T, Henningsson P, Lin H-T. 2016 Flight of the dragonflies and damselflies. *Phil. Trans. R. Soc. B* **371**, 20150389. (doi:10.1098/rstb.2015.0389)
31. Wang ZJ, Russell D. 2007 Effect of forewing and hindwing interactions on aerodynamic forces and power in hovering dragonfly flight. *Phys. Rev. Lett.* **99**, 148101. (doi:10.1103/PhysRevLett.99.148101)
32. Ellington C. 1984 The aerodynamics of hovering insect flight. III. Kinematics. *Phil. Trans. R. Soc. Lond. B* **305**, 41–78. (doi:10.1098/rstb.1984.0051)
33. Zeyghami S, Babu N, Dong H. 2016 Cicada (*Tibicen linnei*) steers by force vectoring. *Theor. Appl. Mech. Lett.* **6**, 107–111. (doi:10.1016/j.taml.2015.12.006)
34. Ennos AR. 1989 The kinematics an daerodynamics of the free flight of some Diptera. *J. Exp. Biol.* **142**, 49–85.
35. Iriarte-Díaz J, Swartz SM. 2008 Kinematics of slow turn maneuvering in the fruit bat *Cynopterus brachyotis*. *J. Exp. Biol.* **211**, 3478–3489. (doi:10.1242/jeb.017590).
36. Ros IG, Bassman LC, Badger MA, Pierson AN, Biewener AA. 2011 Pigeons steer like helicopters and generate down- and upstroke lift during low speed turns. *Proc. Natl Acad. Sci. USA* **108**, 19 990–19 995. (doi:10.1073/pnas.1107519108)
37. Wakeling J, Ellington C. 1997 Dragonfly flight. II. Velocities, accelerations and kinematics of flapping flight. *J. Exp. Biol.* **200**, 557–582.
38. Mukundarajan H, Bardon TC, Kim DH, Prakash M. 2016 Surface tension dominates insect flight on fluid interfaces. *J. Exp. Biol.* **219**, 752–766. (doi:10.1242/jeb.127829)
39. Wan H, Dong H, Gai K. 2015 Computational investigation of cicada aerodynamics in forward flight. *J. R. Soc. Interface* **12**, 20141116. (doi:10.1098/rsif.2014.1116)

40. Koehler C, Liang Z, Gaston Z, Wan H, Dong H. 2012 3D reconstruction and analysis of wing deformation in free-flying dragonflies. *J. Exp. Biol.* **215**, 3018–3027. (doi:10.1242/jeb.069005)
41. Kang C-K, Shyy W. 2013 Scaling law and enhancement of lift generation of an insect-size hovering flexible wing. *J. R. Soc. Interface* **10**, 20130361. (doi:10.1098/rsif.2013.0361)
42. Schlichting HT, Truckenbrodt EA. 1979 *Aerodynamics of the airplane*. New York, NY: McGraw-Hill Companies.
43. Taha HE, Hajj MR, Beran PS. 2014 State-space representation of the unsteady aerodynamics of flapping flight. *Aerosp. Sci. Technol.* **34**, 1–11. (doi:10.1016/j.ast.2014.01.011)
44. Liu G, Dong H, Li C. 2016 Vortex dynamics and new lift enhancement mechanism of wing–body interaction in insect forward flight. *J. Fluid Mech.* **795**, 634–651. (doi:10.1017/jfm.2016.175)
45. Mittal R, Dong H, Bozkurttas M, Najjar F, Vargas A, von Loebbecke A. 2008 A versatile sharp interface immersed boundary method for incompressible flows with complex boundaries. *J. Comput. Phys.* **227**, 4825–4852. (doi:10.1016/j.jcp.2008.01.028)
46. Li C, Dong H. 2017 Wing kinematics measurement and aerodynamics of a dragonfly in turning flight. *Bioinspir. Biomim.* **12**, 026001. (doi:10.1088/1748-3190/aa5761)
47. Jeong J, Hussain F. 1995 On the identification of a vortex. *J. Fluid Mech.* **285**, 69–94. (doi:10.1017/S0022112095000462)
48. Lu Y, Shen GX. 2008 Three-dimensional flow structures and evolution of the leading-edge vortices on a flapping wing. *J. Exp. Biol.* **211**, 1221–1230. (doi:10.1242/jeb.010652)
49. Azuma A, Watanabe T. 1988 Flight performance of a dragonfly. *J. Exp. Biol.* **137**, 221–252.
50. Azuma A, Azuma S, Watanabe I, Furuta T. 1985 Flight mechanics of a dragonfly. *J. Exp. Biol.* **116**, 79–107.
51. Chen YH, Skote M. 2015 Study of lift enhancing mechanisms via comparison of two distinct flapping patterns in the dragonfly *Sympetrum flaveolum*. *Phys. Fluids* **27**, 033604. (doi:10.1063/1.4916204)
52. Wakeling J, Ellington C. 1997 Dragonfly flight. III. Lift and power requirements. *J. Exp. Biol.* **200**, 583–600.
53. May ML. 1991 Dragonfly flight: power requirements at high speed and acceleration. *J. Exp. Biol.* **158**, 325–342.
54. Lehmann F-O. 2009 Wing–wake interaction reduces power consumption in insect tandem wings. *Exp. Fluids* **46**, 765–775. (doi:10.1007/s00348-008-0595-0)
55. Usherwood JR, Lehmann F-O. 2008 Phasing of dragonfly wings can improve aerodynamic efficiency by removing swirl. *J. R. Soc. Interface* **5**, 1303–1307. (doi:10.1098/rsif.2008.0124)
56. Sun M, Huang H. 2007 Dragonfly forewing–hindwing interaction at various flight speeds and wing phasing. *AIAA J.* **45**, 508–511. (doi:10.2514/1.24666)
57. Alexander DE. 1984 Unusual phase relationships between the forewings and hindwings in flying dragonflies. *J. Exp. Biol.* **109**, 379–383.
58. Lehmann F-O. 2008 When wings touch wakes: understanding locomotor force control by wake–wing interference in insect wings. *J. Exp. Biol.* **211**, 224–233. (doi:10.1242/jeb.007575)
59. Rayner JM. 1991 On the aerodynamics of animal flight in ground effect. *Phil. Trans. R. Soc. Lond. B* **334**, 119–128. (doi:10.1098/rstb.1991.0101)
60. Sun M, Lan SL. 2004 A computational study of the aerodynamic forces and power requirements of dragonfly (*Aeschna juncea*) hovering. *J. Exp. Biol.* **207**, 1887–1901. (doi:10.1242/jeb.00969)
61. Norberg RÅ. 1975 Hovering flight of the dragonfly *Aeschna juncea* L., kinematics and aerodynamics. In *Swimming and flying in nature* (eds TY-T Wu, CJ Brokaw, C Brennen), pp. 763–781. Berlin, Germany: Springer.
62. Wang JK, Sun M. 2005 A computational study of the aerodynamics and forewing–hindwing interaction of a model dragonfly in forward flight. *J. Exp. Biol.* **208**, 3785–3804. (doi:10.1242/jeb.01852)
63. Chen YH, Skote M, Zhao Y, Huang WM. 2013 Dragonfly (*Sympetrum flaveolum*) flight: kinematic measurement and modelling. *J. Fluids Struct.* **40**, 115–126. (doi:10.1016/j.jfluidstructs.2013.04.003)
64. Dudley R, Ellington CP. 1990 Mechanics of forward flight in bumblebees: II. Quasi-steady lift and power requirements. *J. Exp. Biol.* **148**, 53–88.
65. Meng X, Sun M. 2016 Wing kinematics, aerodynamic forces and vortex-wake structures in fruit-flies in forward flight. *J. Bionic Eng.* **13**, 478–490. (doi:10.1016/S1672-6529(16)60321-9)
66. Willmott AP, Ellington CP, Thomas AL. 1997 Flow visualization and unsteady aerodynamics in the flight of the hawkmoth, *Manduca sexta*. *Phil. Trans. R. Soc. Lond. B* **352**, 303–316. (doi:10.1098/rstb.1997.0022)
67. Bomphrey RJ, Nakata T, Phillips N, Walker SM. 2017 Smart wing rotation and trailing-edge vortices enable high frequency mosquito flight. *Nature* **544**, 92–95. (doi:10.1038/nature21727)
68. Wakeling J, Ellington C. 1997 Dragonfly flight. I. Gliding flight and steady-state aerodynamic forces. *J. Exp. Biol.* **200**, 543–556.
69. Ellington CP, van den Berg C, Willmott AP, Thomas ALR. 1996 Leading-edge vortices in insect flight. *Nature* **384**, 626–630. (doi:10.1038/384626a0)
70. Song J, Luo H, Hedrick TL. 2014 Three-dimensional flow and lift characteristics of a hovering ruby-throated hummingbird. *J. R. Soc. Interface* **11**, 20140541. (doi:10.1098/rsif.2014.0541)
71. Warrick DR, Tobalske BW, Powers DR. 2009 Lift production in the hovering hummingbird. *Phil. Trans. R. Soc. B* **276**, 3747–3752. (doi:10.1098/rspb.2009.1003)
72. Wang ZJ. 2005 Dissecting insect flight. *Annu. Rev. Fluid Mech.* **37**, 183–210. (doi:10.1146/annurev.fluid.36.050802.121940)